Compact and Lightweight Mid-IR Laser Spectrometer for Balloon-borne Water Vapor Measurements in the UTLS

Manuel Graf[1,3], Philipp Scheidegger[1,2], André Kupferschmid[2], Herbert Looser[1], Thomas Peter[3], Ruud Dirksen[4], Lukas Emmenegger[1], and Béla Tuzson[1]

[1]Laboratory for Air Pollution/Environmental Technology, Empa - Swiss Federal Laboratory for Materials Science and Technology, 8600 Dübendorf, Switzerland
[2]Transport at Nanoscale Interfaces, Empa - Swiss Federal Laboratory for Materials Science and Technology, 8600 Dübendorf, Switzerland
[3]Institute for Atmospheric and Climate Science, ETH Zürich, 8092 Zürich, Switzerland
[4]Deutscher Wetterdienst (DWD)/GCOS Reference Upper Air Network (GRUAN) Lead Center, Lindenberg, Germany

Correspondence: Béla Tuzson (bela.tuzson@empa.ch)

Abstract. We describe the development, characterization and first field deployments of a quantum cascade laser direct absorption spectrometer (QCLAS) for water vapor measurements in the upper troposphere and lower stratosphere. The instrument is sufficiently small ($30 \times 23 \times 11 \, \mathrm{cm}^3$) and lightweight ($3.9 \, \mathrm{kg}$) to be carried by meteorological balloons and used for frequent soundings in the upper troposphere and lower stratosphere (UTLS). The spectrometer is a fully independent system, operating autonomously for the duration of a balloon flight. To achieve the required robustness, while satisfying stringent mass limitations, the concepts for optics and electronics have been fundamentally reconsidered compared to laboratory-based spectrometers. A significant enhancement of the mechanical and optical stability is achieved by integrating a segmented circular multipass cell. The H_2O volume mixing ratio is retrieved by calibration-free evaluation of the spectral data, i.e., only relying on SI-traceable measurements and absorption line parameters. An open-path design reduces the risk of contamination, allows fast response and thus high vertical resolution. Laboratory-based characterization experiments show an agreement within $2\,\%$ to reference measurements and a precision of $0.1\,\%$ under conditions comparable to the UTLS. The instrument successfully performed two balloon-borne test flights up to $28 \, \mathrm{km}$ altitude. In the troposphere, the retrieved spectroscopic data was in excellent agreement with the parallel measurements by a frost point hygrometer (CFH). At higher altitude, the quality of the spectral data remained unchanged, but outgassed water vapor within the instrument enclosure was hindering an accurate measurement of the atmospheric water vapor. Despite this limitation, these test flights demonstrated the successful operation of a laser spectrometer in the UTLS aboard a low-volume meteorological balloon, with the perspective of future highly resolved, accurate and cost-efficient soundings.

1 Introduction

Water vapor is an important climate variable and plays a crucial role in various atmospheric processes from the ground to the upper atmosphere. It affects the Earth's radiative balance, not only in the lower troposphere, but also in the upper troposphere and lower stratosphere (UTLS) (Harries, 1997; Held and Soden, 2000; Solomon et al., 2010; Dessler et al., 2013). The strong

ability of water vapor to absorb infrared radiation makes it the largest contributor to the natural greenhouse effect. At the same time, water vapor is a prerequisite for the formation of clouds, which scatter incoming solar shortwave radiation back to space, thereby increasing the Earth's albedo. In addition, H_2O is the major source of the OH radical in the stratosphere (Hanisco et al.,
25 2001), making it a relevant player in UTLS chemistry. Climate modeling and projections rely on the accurate knowledge of the water vapor abundance throughout the lower and middle atmosphere and on the understanding of the underlying processes that control its spatio-temporal variability. Besides satellite measurements with their large coverage but low vertical resolution, this requires availability of frequent, accurate and highly resolved water vapor concentration measurements. While the humidity measurement near the Earth's surface is a well-established procedure (e.g. using capacitive sensors), the accurate and reliable
30 acquisition in the cold and dry UTLS is incomparably more challenging. Ideally, an instrument should deliver high-precision and long-term comparable results that allow the detection of multiannual trends, and furthermore, provide high accuracy, i.e. traceable absolute concentration (Peter et al., 2006). Therefore, the requirements for an ideal UTLS hygrometer are:

(i) High accuracy ($< 10\,\%$) in the UTLS, i.e. 8–20 km altitude at an effective spatial resolution of a few meters, corresponding to measurements at 1 Hz or faster;

35 (ii) SI-traceability to ensure long-term comparability and to avoid calibration-induced errors;

(iii) Sufficient compactness and low weight to enable flexible and frequent deployment aboard of ordinary meteorological balloons without the need for special permission (4.5 kg or less, depending on the local legislation).

The development of an instrument that simultaneously fulfills all these requirements has proven very difficult, as can be deduced from the significant efforts over the past half century. The required accuracy and weight constraints seem mutually
40 exclusive under the demanding environmental conditions, especially for spectroscopic techniques. In addition, the risk of water vapor self-contamination, owed to the strong adhesive properties of the H_2O molecule, has been a limiting factor, particularly for large instrumentation (Rollins et al., 2014).

Currently, cryogenic frost point hygrometers (CFH/FPH) (Vömel et al., 2016; Hall et al., 2016) are the most established instruments for high-accuracy humidity measurements in the UTLS, however, these are yet themselves not free of uncertainties
45 (Brunamonti et al., 2018; Jorge et al., 2020). Additionally, these devices require a fundamental reconception due to their use of fluoroform (R23, CHF_3) as cooling agent, which must be phased out, according to the Montreal Protocol, because of its high global warming potential (UNEP, 2016). Alternative frost point hygrometers based on thermoelectric cooling (TEC) are currently under development (Sugidachi, 2018; Jorge, 2019).

Beside the CFH approach, numerous spectroscopy-based techniques have also been applied in the past three decades in
50 the UTLS, for example Lyman-α photofragment fluorescence, tunable diode laser, and also mass spectrometry. However, intercomparison campaigns have revealed disagreements that exceed the stated accuracy of the individual instruments (Rollins et al., 2014; Fahey et al., 2014). In addition, all these devices suffer from deployment-related limitations, being either aircraft-based (Silver and Hovde, 1994; Sonnenfroh et al., 1998; May, 1998; Diskin et al., 2002; Zondlo et al., 2010; Dyroff et al., 2015; Thornberry et al., 2014; Buchholz and Ebert, 2018), requiring large balloon gondolae, (Durry et al., 2005; Moreau et al.,
55 2005; Gurlit et al., 2005; Durry et al., 2008), or being restricted to nighttime measurements (Lykov et al., 2011).
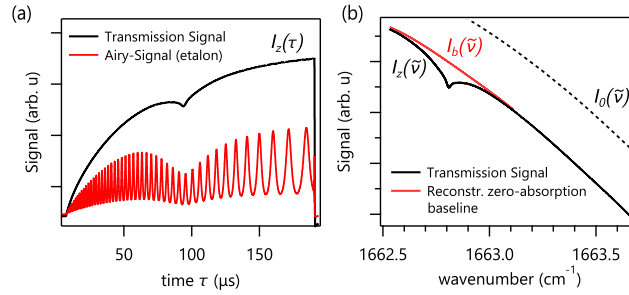
Figure 1. (a) The raw transmission signal through air (black) and a Fabry-Pérot-etalon (red). The Airy signal is used to determine the frequency tuning of the laser. (b) After time-to-frequency conversion, the absorption line is fitted onto a subset of the data. Thereby, the baseline $I_b(\tilde{\nu})$ is reconstructed, which, in contrast to the laser output intensity $I_0(\tilde{\nu})$, includes broadband absorption losses.

In many respects, laser absorption spectroscopy is the method of choice for high-accuracy and contact-free trace gas measurements (Hodgkinson and Tatam, 2013). The advantages lie in the fast acquisition rate, the high molecular specificity and the possibility of calibration-free measurements (Buchholz and Ebert, 2018; Hunsmann et al., 2008), i.e., measurements that are only based on physical parameters such as pressure, temperature and molecule specific spectroscopic data. However, the

60 transition from the laboratory to a balloon-borne instrument is ambitious as it requires a reconsideration of the established concepts. Herein, we describe the development of the first miniaturized, fully standalone mid-IR laser absorption spectrometer for accurate in-situ measurements of water vapor in the UTLS lifted by low-volume meteorological balloons.

2 Methods

2.1 Optical principles

65 The principle of tunable laser direct absorption spectroscopy relies on the excitation of ro-vibrational states of the molecules by a narrow-band light source. In this application, we exploit the fast tunability of a quantum cascade laser to record transmission spectra at kHz repetition rate that cover several wavenumbers. From these spectra, the number density of target molecules is deduced using the Beer-Lambert-law (Eq. 1), which describes the attenuation of radiation in absorbing media. The residual intensity $I_z(\tilde{\nu})$ of a laser beam at wavenumber $\tilde{\nu}$ after passing an optical path length (OPL) z through a homogeneous absorbing

70 medium is expressed by

$$I_z(\tilde{\nu}) = I_0(\tilde{\nu})A(\tilde{\nu},t)\exp(-nz\sigma(\tilde{\nu})), \tag{1}$$

where $n = N/\tilde{V}$ denotes the number density, i.e., the number of absorbing molecules N within a volume $\tilde{V}$. The wavenumber dependence of the absorption coefficient $\sigma(\tilde{\nu})$ can be approximated by a Voigt profile $V(\tilde{\nu};\alpha_D(T),\gamma(p,T))$. The broadening parameters α_D and γ are calculated as a function of the gas pressure p and temperature T using the coefficients from a

75 spectroscopic database. $A(\tilde{\nu},t)$ represents the cumulative broadband transmission losses, e.g., due to windows, finite reflectivity

of mirrors, or the scattering by dust particles or aerosols. This factor may vary over the course of multiple measurements; therefore, it is determined for each spectrum individually. In fact, $AI_0(\tilde{\nu}) = I_b(\tilde{\nu})$ corresponds to the expected signal in absence of absorbing target molecules (Fig. 1a), hereafter referred to as 'baseline'. In laboratory-based closed-cell spectrometers, $I_b(\tilde{\nu})$ can be regularly determined by removing the target species from the measurement volume, e.g., by purging the volume with 'zero-air' or evacuating the absorption cell. Since this is impossible for the herein used open-path system, $I_b(\tilde{\nu})$ is reconstructed during the evaluation procedure of the acquired spectra. Due to the non-linear laser output intensity during the frequency scan (Fig. 1(b)), $I_b(\tilde{\nu})$ is approximated by a polynomial $P_N(\tilde{\nu})$ of the order three to six, depending on the considered spectral range. Since the absorption line shape is fully defined by the absorption coefficient $\sigma(\tilde{\nu})$, the number density n of a particular absorbing species can be determined by minimizing X, i.e. the squared differences between the acquired signal $I_z(\tilde{\nu}_i)$ and the model function. Thereby,

$$X(n, P_N) = \sum_{i=0}^{m} [I_z(\tilde{\nu}_i) - P_N(\tilde{\nu}_i)\exp(-nz\sigma(\tilde{\nu}_i))]^2 \tag{2}$$

is minimized over the m points of the spectrum under variation of n and the polynomial coefficients $p_1 \ldots p_N$ of $P_N = \sum_{j=0}^{N} p_j \tilde{\nu}^j$. Clearly, the reconstruction of P_N becomes more accurate if the data set includes sections far from the line center, i.e., where $\sigma(\tilde{\nu}) \approx 0$. The minimization of X is performed using the Levenberg-Marquardt least-squares algorithm (Press et al., 2007). The spectral line intensity and the broadening parameters are taken from the HITRAN2016 database (Gordon et al., 2017), whereas the actual gas pressure p and temperature T are measured. It is important to note that Eq. 1 establishes a well-defined relation between the (unknown) number density n and the (measured/reconstructed) absorbance $\ln(I_z/I_b)$. The relation only contains directly measurable quantities (T, p, z, I_z) and molecular properties (σ). This renders direct absorption spectroscopy a potentially calibration-free method to determine the number density of a trace gas. The ideal gas law can be applied to calculate the amount of water molecules relative to the number of total molecules, herein expressed as the volume mixing ratio $\chi = n/n_{\text{tot}}$ in units of $\mathrm{mol\,mol^{-1}}$.

In this work, we used the Voigt function to approximate the spectral absorption coefficient $\sigma(\tilde{\nu})$ lack of available parameters for more accurate, higher order profiles. However, the collected data can be reprocessed with more sophisticated line shape models once the corresponding parameters are determined.

Figure 1(a) illustrates a typical raw transmission signal $I_z(\tau)$ as a function of time τ using a quantum cascade laser (QCL) as a light source. The spectral tuning of the QCL is a consequence of the resistive heating of the laser chip exerted by its driving current. Since neither the tuning speed nor the emission intensity are constant over the course of a spectral sweep, the tuning characteristics $\mathrm{d}\tilde{\nu}/\mathrm{d}t$ must be determined for any given driving configuration and operating temperature. This is achieved by recording the Airy transmission signal of a Fabry-Pérot etalon, which yields intensity oscillations with equidistant maxima in wavenumber space. Thereby, the time axis of the raw signal is converted into a wavenumber axis (Fig. 1(b)).

2.2 Absorption line selection

One crucial point in the design of a laser absorption spectrometer is the accurate detection of the absorption signal I_z/I_b, which usually consists of a tiny absorption feature on top of a large background signal. Therefore, the signal-to-noise-ratio (SNR)
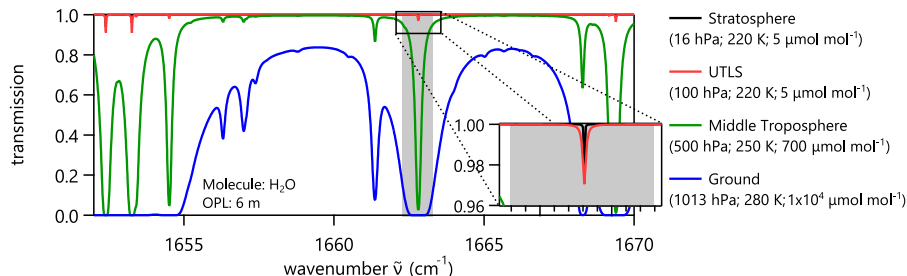
Figure 2. Simulated transmission spectra of H_2O in the mid-IR (around $6\,\mu m$) at several vertical locations of the atmosphere for an absorption path length of $6\,m$. The chosen absorption line is distinctly isolated such that the zero-absorption baseline remains accessible for a broad range of pressures and H_2O concentrations. Its intensity is strong enough to ensure good SNR even at stratospheric conditions. The grayed part denotes the tuning range of the QC laser.

must be sufficiently high to allow the precise determination of the absorption, even at the lowest encountered abundance. There are mainly two fundamental options to enhance the signal: Either by extending the optical path length (OPL) or by selecting a strong absorption line. A long OPL is most frequently achieved using multipass optics, which is often the size-determining component within a spectrometer, while the absorption signal can be optimized by selecting a wavelength range with strong molecular transitions. Many small inorganic molecules exhibit their strongest fundamental transitions in the mid-IR spectral region. H_2O exhibits an absorption band associated to the bending vibration mode (ν_2) around $1600\,cm^{-1}$ ($6\,\mu m$) which is about $30\,\%$ stronger than the absorption band due to the symmetric (ν_1) and asymmetric stretching modes (ν_3) around $3700\,cm^{-1}$ ($2.7\,\mu m$) and about 10 times stronger than the first $\nu_2 + \nu_3$ combination band at around $5300\,cm^{-1}$ ($1.9\,\mu m$). To exploit this advantage and thereby reduce the required OPL, we use a QCL, i.e. a rapidly tunable and powerful semiconductor mid-IR light source (Faist et al., 1994). The target wavelength region has been determined by simulating the transmission spectra of the ν_2-vibration band of water vapor under conditions found during the balloon flight. The selected spectral window is shown in Fig. 2 highlighted in gray, which also corresponds to the spectral coverage of the QCL tuned by current. This window is advantageous since it contains a strong and isolated absorption line ($2_{21} \leftarrow 2_{12}$ at $1662.809\,cm^{-1}$) which facilitates the access to baseline I_b in its vicinity. According to the HITRAN-database, the absorption parameters for this line, especially the intensity, are known with an accuracy better than $2\,\%$ (Birk and Wagner, 2012; Gamache and Hartmann, 2004; Lodi et al., 2011; Toth).

2.3 Instrumentation

2.3.1 Optical layout

The absorption line selected above is best combined with an OPL of $6\,m$ to ensure the SNR to stay above 20 in the lower stratosphere. Such an optical path length can be achieved with a variety of multipass cells (MPCs). However, the choice of
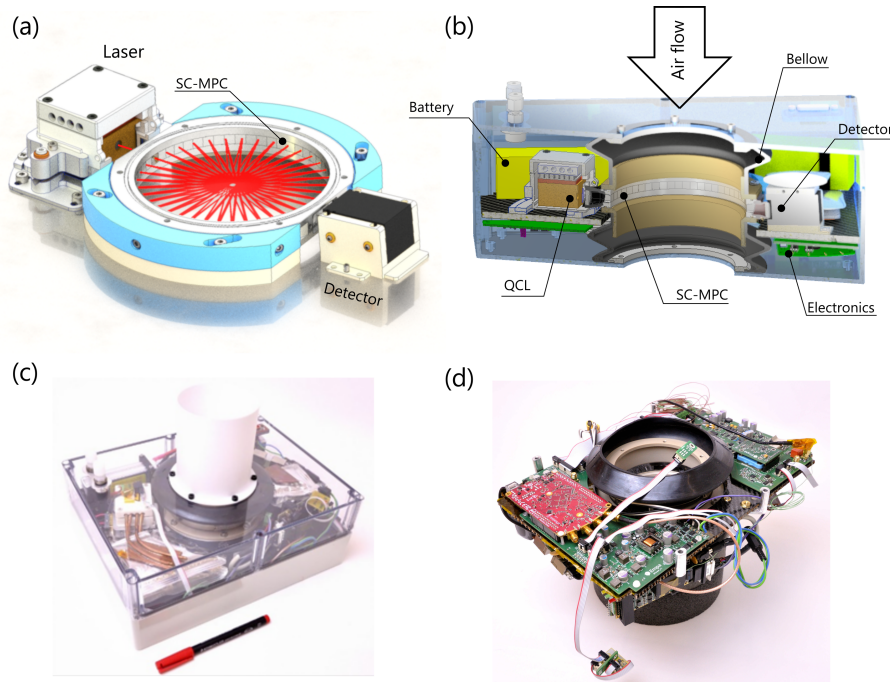
Figure 3. (a) Highly compact optical layout using the segmented circular MPC (SC-MPC), which enables the mounting of laser and detector in direct proximity of its coupling apertures. The beam reflection pattern is schematically depicted by the red trace. (b) Virtual cut showing the integration of our optical concept within the fully assembled spectrometer in open-path configuration. (c) Photo of the fully assembled spectrometer without insulation. (d) Photo of the driving and data acquisition electronics mounted below the optical system.

the MPC is critical for optical and mechanical performance: In fact, there is typically a trade-off between well-controlled and interference-free beam folding, compactness and mechanical stability. We addressed this trade-off by the development of the segmented circular multipass cell (SC-MPC) (Graf et al., 2018), which is schematically shown in Fig. 3(a). This monolithic cell consists of a rotationally symmetric arrangement of individual mirror segments carved into its inner surface. This makes the MPC highly resistant to thermally induced distortion, while the spherical shape of these segments preserves a confined laser beam even upon multiple reflection. In addition, the SC-MPC geometry is well-suited for open-path applications because the air can freely stream perpendicular to the optical plane that contains the star-like reflection pattern.

The cell designed for this instrument weighs $160\,\mathrm{g}$ and contains 57 segments ($6 \times 6\,\mathrm{mm}^2$) which are circularly arranged with a diameter of $108.82\,\mathrm{mm}$. SC-MPCs are tolerant to various input beam shapes, and furthermore, the special curvature of the last segment directly focuses the laser beam onto the detector. Therefore, the collimated laser and the IR detector can be directly attached to the MPC, without the need of additional beam-shaping optics. This enables a compact setup, increases the mechanical stability, and reduces the optical path outside the sampling volume. These features are of general importance for mobile laser spectrometers, as illustrated by Tuzson et al. (2020) for drone based methane detection.

2.3.2 Integration

The instrument incorporates the highly compact optical layout in an open-path configuration, as shown in Fig. 3(a-b). The optics is attached to a lightweight carbon-aramid honeycomb base plate. The air can freely stream through the central funnel that has a minimal diameter of 86 mm. This yields a large flow rate of $30\,\mathrm{l\,s^{-1}}$ upon $5\,\mathrm{m\,s^{-1}}$ ascent rate, which helps reducing the influence of self-contamination caused by water vapor desorbing from the surface. The central funnel is extended by a duct of $10\,\mathrm{cm}$ length (PTFE) preventing contaminated air from the proximity of the instrument to stream through the measurement zone. PTFE is chosen because of its low porosity and its low outgassing rate under reduced pressure (Weissler and Carlson, 1980). In addition, it is hydrophobic and generally non-adhesive, thus preventing the deposition of hydrometeors or condensate at the inlet. Flexible bellows, which tightly connect the MPC with the instrument's enclosure, inhibit the propagation of external stress onto the optical system, while suppressing the convective exchange of cold outside air with the internal volume.

For thermal reasons, the highly temperature sensitive laser and detector are not in direct contact with the MPC, which is fully exposed to the outside air temperature variation. The laser is mounted on a custom-made aluminum alignment stage that allows high-precision positioning along five axes. Having all necessary degrees of freedom covered at the laser side, the mounting of the detector can be kept simple, since the beam alignment is accomplished by adjustments on the laser. Thus, the detector is enclosed by a 3D printed holder that is directly fixed onto the board. The detector holder, which further acts as thermal insulation, is covered by an aluminum plate that is connected to heat pipes and serves as a heat exchanger.

This efficient and compact construction permits the optical plane to be located only $1.75\,\mathrm{cm}$ above the board surface. At this height, the MPC is held in position by 3D printed braces, which are equipped with a heating wire allowing the temperature-control of the cell, e.g., to prevent icing or condensation. The instrument is enclosed in a polycarbonate box. Its lid contains two connections for purging the internal volume with dry gas prior to lift-off. In combination with a $4\,\mathrm{cm}$ thick insulating layer of expanded polystyrol (XPS), the instrument has a total weight of $3.86\,\mathrm{kg}$.

2.3.3 Thermal management

Thermal control and stabilization are of utmost importance for high-precision laser spectrometers. The large temperature variability encountered during a balloon flight to the stratosphere renders this especially challenging. To avoid laser frequency drifts, the temperature of the active region of the QCL must be within a few mK, while the outside air temperature may change by $80\,\mathrm{K}$. In addition, the electronics' excess heat ($\sim 15\,\mathrm{W}$) must be managed. This cannot be done by passive coupling to the outside atmosphere, because of the large temperature span, which would lead to uncontrollable changes in cooling power. In fact, passive coupling would require a variation of the heat transfer coefficient by about one order of magnitude during ascent, in order to keep the heat source at a constant temperature: On ground and above ca. $20\,\mathrm{km}$, efficient cooling is required, while insulation is needed during the rest of the flight to maintain the internal temperature.

Our strategy of thermal management relies on the fact that the instrument has to be stabilized only for a limited amount of time ($\Delta t \approx 2\,\mathrm{h}$), and the direction of heat flow is reversed during flight. These are ideal conditions for the use of a heat buffer. More specifically, the instrument is thermally decoupled from the outside air by the insulating XPS layer mounted around the

enclosure. Sensitive electronic elements are additionally insulated except at one well-defined area of heat exchange. This area is coupled, either directly or via heat pipes, to an organic phase-change material (PCM, RT 18 HC, Rubitherm, Germany) as buffer medium with a phase transition at $T_c = 18\,°C$, which is close to the operating temperature of the laser. This concept adds passive, nonlinear, and bidirectional thermal inertia. With a combined heat capacity of $260\,kJ\,kg^{-1}$ (i.e., $72.2\,W\,h\,kg^{-1}$; latent and specific heat between $11\,°C$ and $26\,°C$) an amount of $416\,g$ PCM is required to fully take up $15\,W$ during $2\,h$. Assuming a bidirectional use, the amount of PCM can be halved. Depending on heat production and tolerable temperature range, the individual electronic components are equipped with $10\text{–}40\,g$ of PCM, encapsulated in custom-made pads. The laser, as the most sensitive device, is additionally stabilized by a PID-controlled TEC, while its heat-sink is also connected to the buffer medium. This combination of active control and increase of thermal inertia successfully limits the variation of the internal air temperature during a balloon flight to $T_0 \pm 10\,K$ and the laser chip to $\Delta T = 19\,mK$ as shown in Fig. 4. The laser temperature variation is derived by its frequency shift, which is determined using the absorption line position as a reference (red trace). At the tropopause, where the line contrast is lowest, i.e., the absorption line is still broad but has a rather small amplitude; the determination of the central frequency is most difficult and thus exhibits the highest noise level.

2.3.4 Laser driving and data acquisition

Most of the custom-developed electronic circuitry boards (PCBs) are integrated on the bottom side of the carbon base plate, as indicated in Fig. 3(d). The core of the electronics system is given by a commercial single board computer 'Red Pitaya' (STEM-Lab, Slovenia). This partly open source hardware features a field programmable gate array (FPGA) and a microcontroller unit (MCU) running a GNU/Linux operating system. The FPGA on Red Pitaya has been reconfigured to provide the functionalities for high-resolution absorption spectroscopy (Liu et al., 2018; Tuzson et al., 2020).

As a light source, we use a distributed feedback quantum cascade laser (DFB-QCL) packaged in a TEC-equipped HHL housing with embedded collimation optics (Alpes Lasers SA, Switzerland). It is operated at a base temperature of $24\,°C$. The rapid spectral sweeping of a QCL is achieved by periodic modulation of the laser driving current. An especially economic strategy is referred to as 'intermittent continuous wave' (ICW) (Fischer et al., 2014), whereby the driving current is applied in pulses, followed by a moment of complete shut-down of the laser to re-establish its initial temperature. In comparison to the generic continuous wave (CW) driving schemes, icw driving drastically reduces the energy consumption and, thus, the production of excess heat. The current ramps are generated by custom-developed analogue electronics (Liu et al., 2018).

For the detection of the laser signal we use a thermoelectrically cooled MCT-detector (PVM-2TE-8 1×1, Vigo System, Poland) coupled to a small-footprint preamplifier (SIP-DC-20M) with a bandwidth of $20\,MHz$. Figure 5 summarizes the data-flow within the instrument. The preamplified raw signal is digitized by a 14-bit analog-digital-converter (ADC) at $125\,MS\,s^{-1}$, which is integrated on Red Pitaya. Since the FPGA also provides the trigger signals for the laser-driving unit, the acquired data can be grouped into single spectra. An individual spectrum is recorded during the applied current ramp that lasts for $200\,\mu s$ and consists of 25'000 data points, followed by a shut-off period of $100\,\mu s$. A dedicated FPGA functionality sums up in real-time a predefined amount of individual spectra – usually a few thousand spectra per second – in order to improve the SNR. The
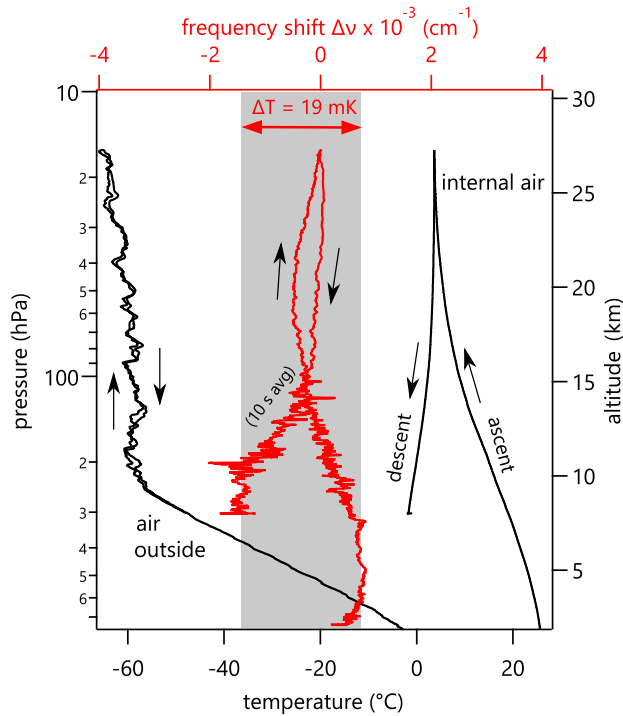
Figure 4. Temperature measurements during the first balloon flight in the UTLS demonstrating the thermal stability of the instrument. The laser temperature variation is derived from its detuning, i.e., the change of the absorption line's central frequency (red, top axis), indicating a maximal temperature drift of $19\,\mathrm{mK}$. This measurement is in relation to the internal and external air temperature (black, bottom axis). The pronounced variability of the laser temperature around the tropopause (300–100 hPa) is caused by the fitting procedure of the central frequency of the absorption line rather than effective temperature changes.

number of averaged spectra and the duty-cycle can be individually selected, taking into account the trade-off between precision, temporal resolution, and covered wavelength range.

210   After completion of the spectral summation, the data set is transferred to the MCU using the internal RAM in a ring-buffer scheme. These data can either be sent to an external computer in real-time via a TCP/IP-interface or, in autonomous operation mode during flight, the spectra are stored on board a flash memory for post-processing. In addition to the fast acquisition of spectra, various sensors and status variables are accessed at $1\,\mathrm{Hz}$ for spectral or diagnostic purposes. The communication, the processing, and the storage of these values is handled by Python software running on the MCU. This concept allows
215   easy implementation of additional features such as laser protection, controlled heating of the MPC or locking of the laser temperature.
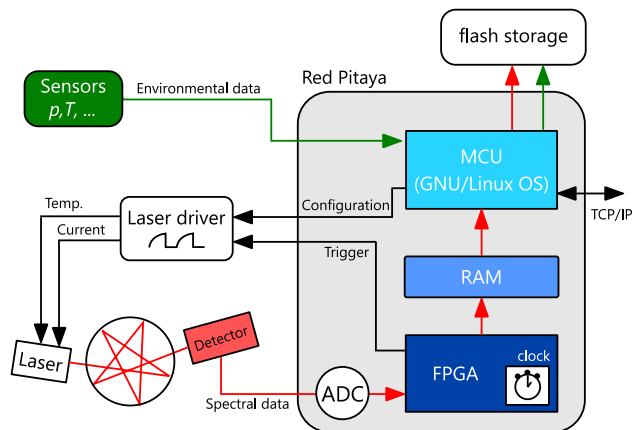
Figure 5. Schematics of data acquisition and transfer within the instrument. To acquire spectral data, the laser driver is triggered by the FPGA and operates according to a given configuration preset defining laser current, temperature, etc. A multitude of additional sensors both for spectroscopic as well as diagnostic purposes (green) are regularly read out. The internal clock of the FPGA synchronizes the different tasks.

3 Validation experiments

3.1 Laboratory-based

The characterization and validation of the spectrometer at representative conditions in the laboratory is highly demanding, given the wide span of temperature, pressure, and water vapor concentration encountered during balloon flights. More specifically, volume mixing ratios χ of $10\,\mu\mathrm{mol\,mol}^{-1}$ and less are very challenging to produce accurately due to the pronounced adsorption properties of H_2O. Similarly, temperatures T of $-70\,°\mathrm{C}$ and pressures p as low as $100\,\mathrm{hPa}$ can only be obtained in specialized climate chambers. Since it was not possible to cover the entire space of occurring p, T, χ in a well-controlled fashion, a subspace of these target conditions was assessed in individual experiments. To characterize the performance at low pressure, the instrument is exposed in open-path configuration to different pressures at room temperature in a home-built pressure chamber. The chamber is continuously purged by H_2O/N_2 mixtures, gravimetrically admixed using a dynamic generator (HCD311, HovaCAL, IAS GmbH, Germany), as depicted in Fig. 6(b). Due to the large surface area of the chamber walls, the lowest achievable H_2O mixing ratio is $2000\,\mu\mathrm{mol\,mol}^{-1}$. To obtain an absorbance representative to the UTLS under these conditions, the measurements are taken at a neighboring absorption line at $\nu_0 = 1665.7\,\mathrm{cm}^{-1}$, which exhibits about three orders of magnitude weaker absorption intensity, as shown in Fig. 6(a).

In a first experiment, the precision of the instrument at constant conditions is assessed using the Allan-Werle-deviation technique (Werle et al., 1993), as shown in Fig. 6(c), where the evolution of precision as a function of the averaging time is quantified. For this measurement, the sampling volume is held at $\chi = 2.3\,\%$, $p = 258.5\,\mathrm{hPa}$, and $T = 296\,\mathrm{K}$ by continuous purging. To ensure stable operation of the instrument for longer period than the targeted $2\,\mathrm{h}$, an externally driven liquid cooling system is used (UC180, Solid State Cooling Systems, USA). Values for the mixing ratio χ are acquired at $1\,\mathrm{Hz}$, after co-
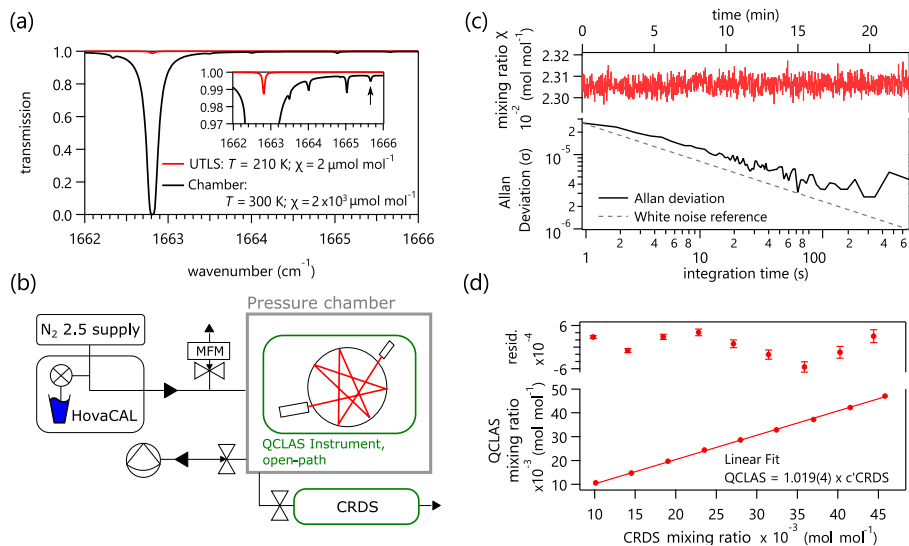
Figure 6. (a) Absorption lines in the vicinity of the one selected for UTLS measurements are about three orders of magnitude weaker, which renders them a representative alternative for measurements at high H_2O concentration. (b) The laboratory-based setup for open-path instrument characterization. (c) Allan-Werle-deviation plot at $259\,\text{hPa}$ for an absorbance representative for the UTLS. A relative Allan deviation of $0.11\,\%$ at $1\,\text{Hz}$ is found, showing further enhancement upon longer averaging times. (d) Direct comparison of the calibration-free QCLAS results with a calibrated CRDS system at $253\,\text{hPa}$, showing excellent agreement with a coefficient of determination $R^2 = 0.9989$).

averaging of 3000 individual spectra. An Allan-Werle-deviation of $26\,\mu\text{mol}\,\text{mol}^{-1}$ ($0.11\,\%$) is obtained at an integration time of $1\,\text{s}$, while an order of magnitude improvement on precision can be achieved by integration over hundred seconds.

In a second experimental series, the accuracy of the instrument is assessed by comparison to the measurements of a commercially available cavity ring-down spectrometer (CRDS; Model G2401, Picarro Inc, USA). The CRDS analyzes extracted air from the chamber within its built-in pressure-controlled cavity held at $200\,\text{hPa}$, thereby setting a lower limit for the range of accessible pressures. Figure 6(d) shows excellent agreement between the QCLAS and the calibrated CRDS at $253\,\text{hPa}$. Calibration of the CRDS was based on a dew-point hygrometer, while the QCLAS results are found by a calibration-free procedure, as discussed above. Additional tests assessing the mechanical and thermal sensitivity have been performed, elaborating the performance of the instrument under field conditions. This includes climate chamber experiments at stratospheric pressure, temperature, and humidity; however, due to technical limitations, without the possibility of controlling more than one of these parameters simultaneously. A detailed discussion of these experiments is given in Graf (2020)

3.2 In-flight test and intercomparison

As a first assessment of the novel QCLAS instrument under realistic conditions, two test flights were performed at Meteorological Observatory Lindenberg, Germany, which also hosts the lead center of the GCOS Reference Upper-Air Network (GRUAN) (Bodeker et al., 2016). The QCLAS was deployed in the UTLS on the 17th and 18th of December 2019. It was

attached with a 45 m rope to a small volume balloon (TX1200, $3\,m^3$) and reached altitudes of 28.3 km and 27.4 km, respectively, on the two consecutive days. Both deployments were accompanied by a parallel ascent of a CFH instrument, serving as reference for the measured H_2O volume mixing ratios. The CFH was launched on a separate balloon to keep the payload below 4 kg. However, the starts were sufficiently close in time to make CFH-QCLAS comparisons meaningful; CFH launches just 37 min and 7 min before the QCLAS for Flight I and Flight II, respectively. During Flight II, the CFH data showed a clear and strong contamination-associated offset, especially above the tropopause, after ascending through a 800 m thick layer with RH > 98.5 %. Therefore, we focus here on the evaluation and comparison of the first flight, where the complete ascent and descent data sets are available from both instruments. For the spectroscopic retrieval of the H_2O mixing ratios, the p and T values are used from an attached RS41 radiosonde (Vaisala, Finnland). Taking the values from the standardized and well-characterized radiosonde is preferred over the use of the system-integrated sensors, since temperature measurements are highly delicate under these conditions and strongly depend on the specific integration properties of the T-sensor (Shimizu and Hasebe, 2010). The descent data stops as soon as the ground station has lost the signal to the RS41, even though the QCLAS continues to operate to 5 km altitude. The instrument was recovered using the GPS coordinates received from the radiosonde. The spectra were recorded at a repetition period of $300\,\mu s$, which is a good trade-off between broad spectral coverage and scanning speed as it enables the co-averaging of 3000 spectra to reach 1 Hz temporal and 5 m vertical resolution.

3.2.1   Results and discussion

Figure 7(a) shows the vertical profile of H_2O mixing ratios from both instruments for ascending and descending measurements over the available range of altitudes. Figure 7(b) focuses on the troposphere, where the results from the QCLAS are in excellent agreement with the CFH. The mean deviation is only 3% and the values remain close even when the absorption line is already partly saturated. In the right panel of this figure, the relative deviation is plotted, showing a standard deviation of 13 % between 2 and 10 km altitude. Large differences are observed around sudden changes in the humidity profile caused by natural short-scale spatio-temporal variations in the tropospheric moisture. The deviations between both instruments can be due to the slightly different flight trajectories, and the faster response time of the QCLAS compared to the CFH.

Above ca. 10 km altitude, the QCLAS gradually retrieves higher H_2O mixing ratios compared to the CFH. This is attributed to the enhanced outgassing of water vapor from the internal surfaces of the instrument over the course of the flight. This water vapor interacts with the laser beam within the short optical path (9 mm) between the laser/detector and the cell entrance and thus, contributes to the total absorption. Although, this internal OPL is only 0.14 % of the total OPL, the corresponding light absorption can still generate a significant offset in the data with increasing altitude. For example, a superposition of the atmospheric absorption due to $5\,\mu mol\,mol^{-1}$ water vapor at 20 km altitude (50 hPa) and the internal absorption by $10^4\,\mu mol\,mol^{-1}$ H_2O over 0.14 % of the total OPL at similar pressure, results in an apparent mixing ratio of $19\,\mu mol\,mol^{-1}$. This bias could not even be avoided by thoroughly flushing the instrument with dry nitrogen prior to lift-off. An attempt to correct this bias by measuring the internal humidity with a low-cost capacitive sensor is shown as the blue curve for the QCLAS descent data. For better comparison to CFH, a 20 s moving average filter is applied to this curve. While this correction partly removes the trend, the sensor fails to deliver plausible absolute values in the stratosphere, where the environmental conditions (p < 200 hPa,
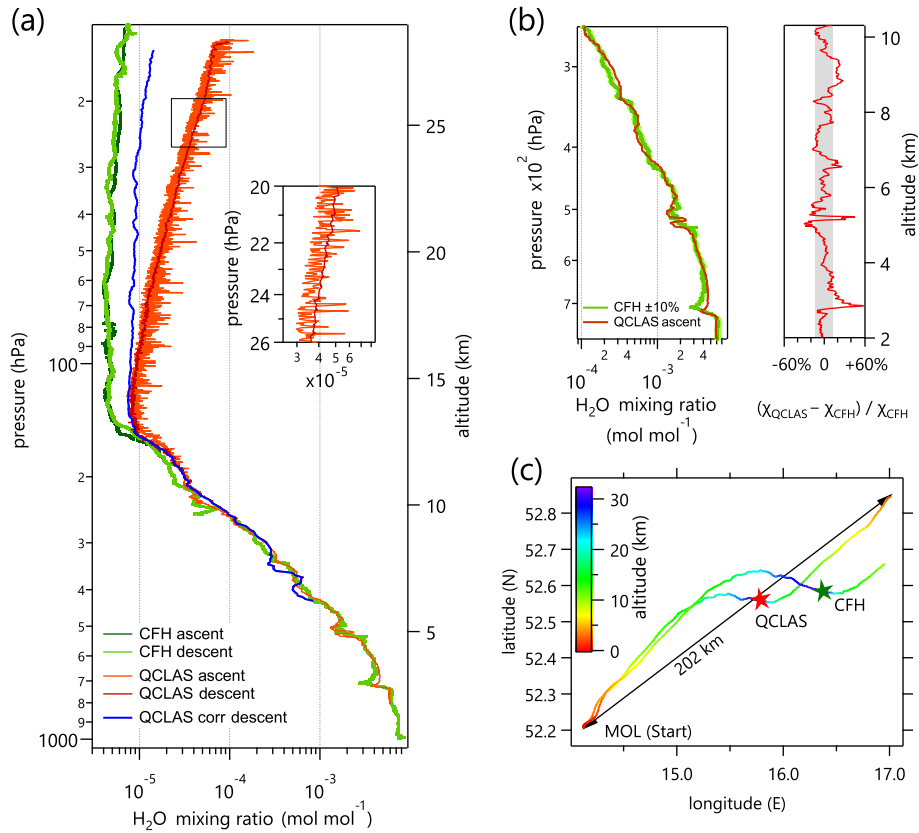
Figure 7. (a) H_2O volume mixing ratio profiles measured by QCLAS and CFH during ascent and descent. The inset shows the unilateral spikes on top of a slowly varying signal in the stratosphere. An attempt to correct for the spurious absorption caused by the 0.14 % section of internal OPL is shown as blue curve (see main text for details). (b) Close-up of the tropospheric measurements; the relative deviation is plotted in the right panel, showing a standard deviation of 13 % (gray area) among the instruments. (c) Flight trajectories and burst points – the two balloons were launched with a time lag of 37 min.

RH < 8 %) are far beyond the specifications for this capacitive RH-sensor. Therefore, it is likely that the remaining bias between CFH and the corrected QCLAS data is caused by a significant error of the internal humidity measurement.

This problem of internal outgassing is therefore to be addressed in the near future by a technical adaptation: Either by completely eliminating the internal optical path or by establishing a pressure difference within the instrument with respect to the surrounding atmosphere. The latter may be achieved by a leak-tight channel around the internal section of the laser beam that allows to maintain ground pressure in this compartment during the flight. This would allow the spectroscopic disentanglement of the absorption features due to the different pressure broadening. A strategy that is currently applied successfully to distinguish the contribution of residual humidity within the HHL housing of the laser: Figure 8 shows an in-flight spectrum recorded at 13.8 km altitude, i.e., at the hygropause. The narrow absorption feature due the atmospheric and instrument-internal humidity at low pressure (141 hPa) is superimposed over a broad feature that originates from residual moisture within the enclosure
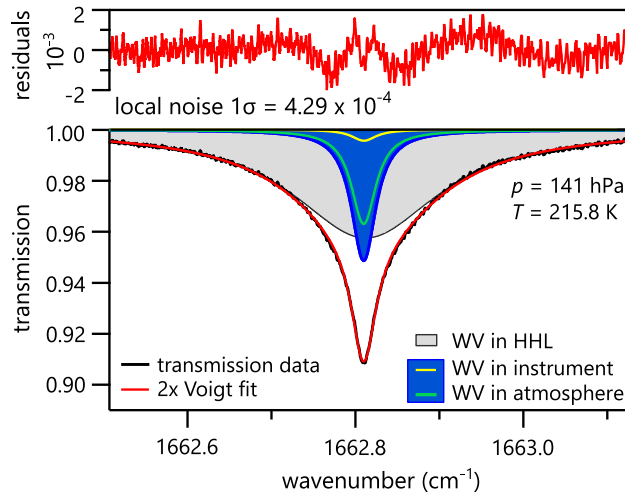
Figure 8. Representative transmission spectrum recorded during balloon-borne deployment at $13.8\,\mathrm{km}$ altitude. The spectrum exhibits two spectroscopically distinguishable features: a broad absorption (gray) due to the enclosed water vapor within the laser housing HHL (OPL of $3\,\mathrm{mm}$) at ca. $1000\,\mathrm{hPa}$ and a narrow absorption (blue) at a pressure of $141\,\mathrm{hPa}$. The latter feature is again a superposition of two contributions: the atmospheric absorption (green) within the MPC (OPL of $6\,\mathrm{m}$ and $T = 215.8\,\mathrm{K}$) as well as the absorption by trapped water vapor within the instrument's enclosure, which is not distinguishable spectroscopically (yellow).

295 of the laser at ground pressure. This OPL is of approximately $3\,\mathrm{mm}$ corresponding to the distance between the laser chip facet and the window of the HHL housing. Because of the leak-tight sealing of the laser enclosure, the pressure remains constant during flight, therefore allowing the precise disentanglement of these contributions due to their unequal pressure broadening, especially at high altitude. In the evaluation procedure, we account for this effect by the simultaneous fitting of two absorption line profiles at their corresponding pressure.

300   Apart from the offset due to internal humidity, the ascent data shows distinct spikes with an amplitude of up to $40\,\mu\mathrm{mol\,mol^{-1}}$ on top of a slowly varying signal above the tropopause at about $10\,\mathrm{km}$ altitude. A close-up of this structure is presented as an inset in Fig. 7(a). A Fourier transform analysis indicates a preferred occurrence of these spikes with periodicities of $\tau_1 = 6.5\,\mathrm{s}$ and $\tau_2 = 12.4\,\mathrm{s} \approx 2\tau_1$. Assuming a gravitational pendulum as an idealized model describing the instrument's motion below the balloon, the expected periodicity would be $\tau_p = 2\pi\sqrt{L/g} = 13.5\,\mathrm{s}$ for the used rope length $L = 45\,\mathrm{m}$. In accordance with

305 Jorge et al. (2020), who analyzed the GPS data of balloon soundings, it is thus plausible that these spikes are caused by repeated transitions of the instrument through the wake of the balloon in an oscillating fashion. This hypothesis is strongly supported by the fact that the spikes immediately disappear after the burst of the balloon, indicating that they are balloon-associated rather than originating from the enclosure of the instrument. Possible reasons for the absence of a similar effect in the CFH data are the lower temporal resolution and the longer rope ($60\,\mathrm{m}$) for the CFH. The quantitative contribution of these individual

310 factors is difficult to estimate, but will be investigated during future test flights of the QCLAS. Most importantly, however, any balloon-related contamination can be avoided by measuring during descent (Kräuchi et al., 2016), which is perfectly feasible
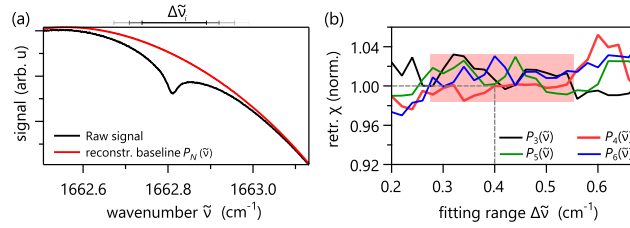
Figure 9. (a) Fitting of the measured transmission data. The choice of the baseline polynomial (red) and the selected range $\Delta\tilde{\nu}_i$ to evaluate a measured spectrum need to be optimized. Varying these parameters can influence the retrieved H_2O mixing ratio χ, as shown in (b) after repeated evaluation of the same spectrum. Good agreement among the polynomial degrees over broad range of fitting ranges is found. Within the red highlighted region, the standard deviation of all fitting results amounts to 1.1 % relative to the finally selected configuration for the analysis of the data: $\Delta\tilde{\nu} = 0.4\,\text{cm}^{-1}$ and $P_4(\tilde{\nu})$.

due to our instrument's high gas exchange rate and its high temporal resolution capabilities. It is important to note that the higher mixing ratio, which is measured upon descent in the stratosphere, is a consequence of the internally trapped water vapor: The internal concentration continues to increase during the first 3 km of descent due to further desorption.

3.2.2 Uncertainty assessment

In the UTLS, the biases discussed above inhibit the assessment of the accuracy by direct comparison to CFH. Therefore, to quantify the expected accuracy of our spectrometer, we compiled a bottom-up uncertainty budget and discuss the relevant contributions. These sources of uncertainty may be grouped into four categories:

(0) **spurious water vapor (external and internal)**: These contributions are discussed in the previous section. They are to be avoided by technical adaptations on the instrument and the deployment system.

(i) **measurement related uncertainties**: The relative uncertainty of the T and p measurements by the RS41 radiosonde is specified to 0.2 % and 0.5 % (Vaisala, 2020), respectively.

(ii) **thermally induced variations**: The thermal expansion/contraction of the MPC during the flight, due to a temperature variation of 54 K, induces a change of 0.12 % in the OPL. Since thermal expansion is a simple function of temperature, this effect could, in principle, be included in the evaluation procedure. However, this small effect was not taken into consideration during the data processing. In contrast to the thermal expansion, variations of the laser temperature can lead to changes that are more difficult to quantify. Although, the thermal management system successfully stabilizes the laser temperature within 19 mK during the entire flight (see Fig. 4), the residual change in the laser temperature still causes a frequency shift of $3 \times 10^{-3}\,\text{cm}^{-1}$. This may lead to a variation of the laser's tuning characteristics that were determined prior the flight using a Fabry-Pérot etalon. Corresponding calculations indicate a maximum change of 0.76 % in the derived mixing ratio during the entire flight.

(iii) **uncertainties of the spectroscopic retrieval**: For the retrieval of the water vapor mixing ratio based on the recorded spectra, an important source of uncertainty is the limited accuracy of the line parameters given in the spectral database, i.e., 1–2 % on the line intensity and 1 % on the pressure-broadening coefficient. For comparison, the normalized spectral noise level

(1σ) of 4.3×10^{-4} has a negligible contribution to the total uncertainty, i.e., 0.1 % at 1 s as indicated by the Allan-deviation plot.

However, the retrieved concentrations show a slight dependence on the fitting configuration, e.g. the spectral window size $\Delta\tilde{\nu}$ and the chosen polynomial order N, used for the reconstruction of the spectral baseline (see Fig. 9(a)). In order to quantify the robustness of the fitting procedure and the sensitivity of the retrieved concentration on the selection of $\Delta\tilde{\nu}$ and $P_N(\tilde{\nu})$, the same spectrum is evaluated with different fitting configurations, as shown in Fig. 9(b). This comparison is performed for spectra at different altitudes. As expected, the variation of the mixing ratio χ among different fitting presets is highest when the contrast of the absorption line is low, i.e. the height of the absorption feature divided by its width is small. This is particularly the case at the hygropause, where the ambient pressure is still relatively high, while the H_2O abundance is very low (see Fig. 8). Nevertheless, even for low contrast spectra, the deviations remain small within a reasonable range of fitting configurations. The evaluated mixing ratios χ reach a stable plateau in the region $\Delta\tilde{\nu} = 0.4\,\mathrm{cm}^{-1}$ for baseline polynomials of the order 3 to 6. Within this region (red area), the calculated χ show a standard deviation of only 1.1 %. Therefore, the central values $\Delta\tilde{\nu} = 0.4\,\mathrm{cm}^{-1}$ and $P_4(\tilde{\nu})$ are the selected evaluation settings to analyze the presented experimental data. In Fig. 8(b), the mixing ratio retrieved with this configuration is set to unity. Other combinations within the red area show maximal deviations of +3.2% and -1.2%.

Based on the contributions discussed here, the total instrument-intrinsic uncertainty (i-iii) amounts to 2.5 %. This budget does, however, not include the error that may be induced by the fact that the Voigt profile does not describe ro-vibrational transitions in their full complexity (Ngo et al., 2013; Tran et al., 2013). This manifests itself as a characteristic W-shaped structure in the residuals (see Fig. 8) that changes with pressure. For certain near-IR transitions, deviations of 2–5 % in the absorption line integral have been found between a simple Voigt, and higher-order profiles (Lisak et al., 2015). However, these are exceptional cases, which are chosen to illustrate the benefit of elaborate line shape models. Therefore, they likely represent an upper limit of disagreement and require up to five fitting parameters, which are currently not available for the molecular transition used here. Nevertheless, future experiments should include a detailed investigation of the herein selected absorption line to determine the missing parameters for a more sophisticated line shape model.

3.3 Outlook

The signal bias due to internal humidity and the high uncertainty of its correction currently inhibits a definitive confirmation of the stated uncertainty budget. Therefore, it is of highest importance to eliminate the influence of the internal optical path by a constructional adaption. Once this source of error is removed, it will be possible to quantify the accuracy of the instrument by comparison to CFH and to proof the absence of instrument-associated contamination that we sought to minimize by the open-path construction of the instrument. Such future comparison flights, where the use of longer ropes is clearly indicated, will be supplemented by laboratory-based experiments as well as the participation in intercomparsion campaigns to further characterize the performance of this instrument under realistic conditions.

4 Conclusions

This work describes the development of a compact QCL-based direct absorption spectrometer (3.9 kg) for the measurement of water vapor in the UTLS aboard of meteorological balloons. It relies on an open-path segmented circular MPC and includes specifically developed hardware, such as laser driver electronics and FPGA-based data acquisition, as well as dedicated controlling software. A tailored thermal stabilization system based on a combination of phase-change material and thermo-electric cooling allows the autonomous operation of the instrument during balloon-carried ascents and subsequent descents on a parachute. The open-path design prevents self-contamination due to tubing and pumps, and it enables a very fast response time, which is confirmed by the identification of individual wake transitions during balloon-borne ascent. Laboratory experiments show a precision of 0.1 % and excellent agreement with a CRDS instrument, supporting the calibration-free evaluation approach. Comparison to a CFH, flown simultaneously on a separate balloon, reveals a relative average deviation of 3 % in the troposphere. The accuracy of the stratospheric measurements is currently limited by outgassed water vapor within the enclosure of the instrument, which leads to a bias of the measured concentration at high altitude. Apart from this issue, which should be amendable by constructional adaptations, the system demonstrated highly stable operation even in the stratosphere. In conclusion, we measured UTLS water vapor using a lightweight and standalone mid-IR spectrometer, which is a promising candidate for future high-accuracy assessments of UTLS water vapor on a regular basis.

Data availability. The data used in this manuscript are available from the corresponding author upon request.

Author contributions. M.G. designed and developed the instrument, collected and evaluated the data under the supervision of B.T. who managed the project together with L.E. and T.P. P.S. designed and developed the electronics hardware. A.K. developed and implemented FPGA and DAQ functionalities. H.L. developed analysis software. R.D. provided support to launch from Lindenberg. M.G. prepared the manuscript with contributions from all authors.

Competing interests. The authors declare that they have no conflict of interest.

Acknowledgements. The authors kindly acknowledge Badrudin Stanicki and Killian Brennan for their technical support, Curdin Flepp and Florian Lienhard for their contribution in software development. Further, many thanks to Tobias Bühlmann from METAS for his help with the laboratory characterization experiments. Special thanks to the GRUAN team at DWD Lindenberg, in particular Sabine Körner, for their support with the balloon launches and instrument recovery. We also thank Erwin Pieper and Urs Hintermüller from the mechanical engineering workshop at Empa for their support and the helpful discussions. This project has received funding from the Swiss National Science Foundation (SNSF) under grant agreement nr. 157208.

References

Birk, M. and Wagner, G.: Temperature-dependent air-broadening of water in the $1250\check{}1750\,\mathrm{cm}^{-1}$ range, Journal of Quantitative Spectroscopy and Radiative Transfer, 113, 889–928, https://doi.org/10.1016/j.jqsrt.2011.12.013, 2012.

Bodeker, G. E., Bojinski, S., Cimini, D., Dirksen, R. J., Haeffelin, M., Hannigan, J. W., Hurst, D. F., Leblanc, T., Madonna, F., Maturilli, M., Mikalsen, A. C., Philipona, R., Reale, T., Seidel, D. J., Tan, D. G. H., Thorne, P. W., Vömel, H., and Wang, J.: Reference Upper-Air Observations for Climate: From Concept to Reality, Bulletin of the American Meteorological Society, 97, 123–135, https://doi.org/10.1175/BAMS-D-14-00072.1, 2016.

Brunamonti, S., Jorge, T., Oelsner, P., Hanumanthu, S., Singh, B. B., Ravi Kumar, K., Sonbawne, S., Meier, S., Singh, D., Wienhold, F. G., Ping Luo, B., Boettcher, M., Poltera, Y., Jauhiainen, H., Kayastha, R., Karmacharya, J., DIrksen, R., Naja, M., Rex, M., Fadnavis, S., and Peter, T.: Balloon-borne measurements of temperature, water vapor, ozone and aerosol backscatter on the southern slopes of the Himalayas during StratoClim 2016-2017, Atmos. Chem. Phys., 18, 15 937–15 957, https://doi.org/10.5194/acp-18-15937-2018, 2018.

Buchholz, B. and Ebert, V.: Absolute, pressure-dependent validation of a calibration-free, airborne laser hygrometer transfer standard (SEALDH-II) from 5 to 1200 ppmv using a metrological humidity generator, Atmos. Meas. Tech., 11, 459–471, https://doi.org/10.5194/amt-11-459-2018, 2018.

Dessler, A. E., Schoeberl, M. R., Wang, T., Davis, S. M., and Rosenlof, K. H.: Stratospheric water vapor feedback, Proc. Natl. Acad. Sci. U. S. A., 110, https://doi.org/10.1073/pnas.1310344110, 2013.

Diskin, G. S., Podolske, J. R., Sachse, G. W., and Slate, T. A.: Open-path airborne tunable diode laser hygrometer, Int. Symp. Opt. Sci. Technol., 4817, 196–204, https://doi.org/10.1117/12.453736, http://proceedings.spiedigitallibrary.org/proceeding.aspx?articleid=1314316, 2002.

Durry, G., Zeninari, V., Parvitte, B., Le Barbu, T., Lefevre, F., Ovarlez, J., and Gamache, R. R.: Pressure-broadening coefficients and line strengths of H_2O near 1.39 μm: Application to the in situ sensing of the middle atmosphere with balloonborne diode lasers, J. Quant. Spectrosc. Radiat. Transf., 94, 387–403, https://doi.org/10.1016/j.jqsrt.2004.09.033, 2005.

Durry, G., Amarouche, N., Joly, L., Liu, X., Parvitte, B., and Zeninari, V.: Laser diode spectroscopy of H_2O at 2.63 um for atmospheric applications, Appl. Phys. B Lasers Opt., 90, 573–580, https://doi.org/10.1007/s00340-007-2884-3, 2008.

Dyroff, C., Sanati, S., Christner, E., Zahn, A., Balzer, M., Bouquet, H., McManus, J. B., Gonzalez-Ramos, Y., and Schneider, M.: Airborne in situ vertical profiling of $HDO/H_2^{16}O$ in the subtropical troposphere during the MUSICA remote sensing validation campaign, Atmos. Meas. Tech., 8, 2037–2049, https://doi.org/10.5194/amt-8-2037-2015, 2015.

Fahey, D. W., Gao, R. S., Möhler, O., Saathoff, H., Schiller, C., Ebert, V., Krämer, M., Peter, T., Amarouche, N., Avallone, L. M., Bauer, R., Bozóki, Z., Christensen, L. E., Davis, S. M., Durry, G., Dyroff, C., Herman, R. L., Hunsmann, S., Khaykin, S. M., Mackrodt, P., Meyer, J., Smith, J. B., Spelten, N., Troy, R. F., Vömel, H., Wagner, S., and Wienhold, F. G.: The AquaVIT-1 intercomparison of atmospheric water vapor measurement techniques, Atmos. Meas. Tech., 7, 3177–3213, https://doi.org/10.5194/amt-7-3177-2014, 2014.

Faist, J., Capasso, F., Sivco, D., Sirtori, C., Hutchinson, A., and Cho, A.: Quantum cascade laser, Science, 264, 553–556, https://doi.org/10.1126/science.264.5158.553, 1994.

Fischer, M., Tuzson, B., Hugi, A., Brönnimann, R., Kunz, A., Blaser, S., Rochat, M., Landry, O., Müller, A., and Emmenegger, L.: Intermittent operation of QC-lasers for mid-IR spectroscopy with low heat dissipation: tuning characteristics and driving electronics, Opt. Express, 22, 7014–7027, https://doi.org/10.1364/OE.22.007014, 2014.

Gamache, R. and Hartmann, J.-M.: An intercomparison of measured pressure-broadening and pressure-shifting parameters of water vapor, Canadian Journal of Chemistry, 82, 1013–1027, https://doi.org/10.1139/v04-069, 2004.

430 Gordon, I., Rothman, L., Hill, C., Kochanov, R., Tan, Y., Bernath, P., Birk, M., Boudon, V., Campargue, A., Chance, K., Drouin, B., Flaud, J.-M., Gamache, R., Hodges, J., Jacquemart, D., Perevalov, V., Perrin, A., Shine, K., Smith, M., Tennyson, J., Toon, G., Tran, H., Tyuterev, V., Barbe, A., Császár, A., Devi, V., Furtenbacher, T., Harrison, J., Hartmann, J.-M., Jolly, A., Johnson, T., Karman, T., Kleiner, I., Kyuberis, A., Loos, J., Lyulin, O., Massie, S., Mikhailenko, S., Moazzen-Ahmadi, N., Müller, H., Naumenko, O., Nikitin, A., Polyansky, O., Rey, M., Rotger, M., Sharpe, S., Sung, K., Starikova, E., Tashkun, S., Auwera, J. V., Wagner, G., Wilzewski, J.,

435 Wcisło, P., Yu, S., and Zak, E.: The HITRAN2016 molecular spectroscopic database, J. Quant. Spectrosc. Radiat. Transf., 203, 3–69, https://doi.org/10.1016/j.jqsrt.2017.06.038, 2017.

Graf, M.: Balloon-borne Atmospheric Water Vapor Measurement by Laser Absorption Spectroscopy, Ph.D. thesis, ETH Zurich, Zurich, 2020.

Graf, M., Emmenegger, L., and Tuzson, B.: Compact, circular, and optically stable multipass cell for mobile laser absorption spectroscopy,

440 Opt. Lett., 43, 2434–2437, https://doi.org/10.1364/OL.43.002434, 2018.

Gurlit, W., Zimmermann, R., Giesemann, C., Fernholz, T., Ebert, V., Wolfrum, J., Platt, U., and Burrows, J. P.: Lightweight diode laser spectrometer CHILD (Compact High-altitude In-situ Laser Diode) for balloonborne measurements of water vapor and methane., Appl. Opt., 44, 91–102, https://doi.org/10.1364/AO.44.000091, 2005.

Hall, E. G., Jordan, A. F., Hurst, D. F., Oltmans, S. J., Vömel, H., Kühnreich, B., and Ebert, V.: Advancements, measurement uncertainties,

445 and recent comparisons of the NOAA frostpoint hygrometer, Atmos. Meas. Tech. Discuss., 2003, 1–29, https://doi.org/10.5194/amt-2016-160, http://www.atmos-meas-tech-discuss.net/amt-2016-160/, 2016.

Hanisco, T. F., Lanzendorf, E. J., Wennberg, P. O., Perkins, K. K., Stimpfle, R. M., Voss, P. B., Anderson, J. G., Cohen, R. C., Fahey, D. W., Gao, R. S., Hintsa, E. J., Salawitch, R. J., Margitan, J. J., McElroy, C. T., and Midwinter, C.: Sources, sinks, and the distribution of OH in the lower stratosphere, J. Phys. Chem. A, 105, 1543–1553, https://doi.org/10.1021/jp002334g, 2001.

450 Harries, J. E.: Atmospheric radiation and atmospheric humidity, Q. J. R. Meteorol. Soc. Part B, 123, 2173–2186, 1997.

Held, I. M. and Soden, B. J.: Water Vapor Feedback And Global Warming, Annu. Rev. Energy Env., 25, 441, 2000.

Hodgkinson, J. and Tatam, R. P.: Optical gas sensing: a review, Meas. Sci. Technol., 24, 012 004, https://doi.org/10.1088/0957-0233/24/1/012004, 2013.

Hunsmann, S., Wunderle, K., Wagner, S., Rascher, U., Schurr, U., and Ebert, V.: Absolute, high resolution water transpiration rate mea-

455 surements on single plant leaves via tunable diode laser absorption spectroscopy (TDLAS) at 1.37 um, Appl. Phys. B Lasers Opt., 92, 393–401, https://doi.org/10.1007/s00340-008-3095-2, 2008.

Jorge, T.: Developments in balloon-borne water vapour measurements with frost point hygrometers, Ph.D. thesis, ETH Zurich, Zurich, https://doi.org/10.3929/ethz-b-000411391, 2019.

Jorge, T., Brunamonti, S., Poltera, Y., Wienhold, F. G., Luo, B. P., Oelsner, P., Hanumanthu, S., Sing, B. B., Körner, S., Dirksen, R.,

460 Naja, M., Fadnavis, S., and Peter, T.: Understanding cryogenic frost point hygrometer measurements after contamination by mixed-phase clouds, Atmospheric Measurement Techniques Discussions, 2020, 1–76, https://doi.org/10.5194/amt-2020-176, https://www.atmos-meas-tech-discuss.net/amt-2020-176/, 2020.

Kräuchi, A., Philipona, R., Romanens, G., Hurst, D. F., Hall, E. G., and Jordan, A. F.: Controlled weather balloon ascents and descents for atmospheric research and climate monitoring, Atmos. Meas. Tech., 9, 929–938, https://doi.org/10.5194/amt-9-929-2016, 2016.

465   Lisak, D., Cygan, A., Bermejo, D., Domenech, J. L., Hodges, J. T., and Tran, H.: Application of the Hartmann-Tran profile to analysis of H2O spectra, J. Quant. Spectrosc. Radiat. Transf., 164, 221–230, https://doi.org/10.1016/j.jqsrt.2015.06.012, 2015.

Liu, C., Tuzson, B., Scheidegger, P., Looser, H., Bereiter, B., Graf, M., Hundt, M., Aseev, O., Maas, D., and Emmenegger, L.: Laser driving and data processing concept for mobile trace gas sensing: Design and implementation, Rev. Sci. Instrum., 89, https://doi.org/10.1063/1.5026546, http://dx.doi.org/10.1063/1.5026546, 2018.

470   Lodi, L., Tennyson, J., and Polyansky, O.: A global, high accuracy *ab initio* dipole moment surface for the electronic ground state of the water molecule, Journal of Chemical Physics, 135, 034113, https://doi.org/10.1063/1.3604934, 2011.

Lykov, A., Yushkov, V., Khaykin, S., Astakhov, V., and Budovich, V.: New version of balloon hygrometer for in situ water vapour measurements in the upper troposphere and lower stratopshere (FLASH-BM), Eur. Sp. Agency, (Special Publ. ESA SP), 700 SP, 341–345, 2011.

475   May, R. D.: Open-path, near-infrared tunable diode laser spectrometer for atmospheric measurements of H2O, J. Geophys. Res. Atmos., 103, 19 161–19 172, https://doi.org/10.1029/98JD01678, 1998.

Moreau, G., Robert, C., Catoire, V., Chartier, M., Camy-Peyret, C., Huret, N., Pirre, M., Pomathiod, L., and Chalumeau, G.: SPIRALE: a multispecies in situ balloonborne instrument with six tunable diode laser spectrometers, Appl. Opt., 44, 2005.

Ngo, N. H., Lisak, D., Tran, H., and Hartmann, J. M.: An isolated line-shape model to go beyond the Voigt profile in spectroscopic databases 480   and radiative transfer codes, J. Quant. Spectrosc. Radiat. Transf., 129, 89–100, https://doi.org/10.1016/j.jqsrt.2013.05.034, 2013.

Peter, T., Marcolli, C., Spichtinger, P., Corti, T., Baker, M. B., and Koop, T.: Atmosphere. When dry air is too humid., Science, 314, 1399–402, https://doi.org/10.1126/science.1135199, 2006.

Press, W. H., Teukolsky, S. A., Vetterling, W. T., and Flannery, B. P.: Numerical Recipes 3rd Edition: The Art of Scientific Computing, Cambridge University Press, USA, 3 edn., 2007.

485   Rollins, A. W., Thornberry, T. D., Gao, R. S., Smith, J. B., Sayres, D. S., Sargent, M. R., Schiller, C., Krämer, M., Spelten, N., Hurst, D. F., Jordan, A. F., Hall, E. G., Vömel, H., Diskin, G. S., Podolske, J. R., Christensen, L. E., Rosenlof, K. H., Jensen, E. J., and Fahey, D. W.: Evaluation of UT/LS hygrometer accuracy by intercomparison during the NASA MACPEX mission, J. Geophys. Res. Atmos., 119, 1915–1935, https://doi.org/10.1002/2013JD020817, 2014.

Shimizu, K. and Hasebe, F.: Fast-response high-resolution temperature sonde aimed at contamination-free profile observations, Atmo-490   spheric Measurement Techniques, 3, 1673–1681, https://doi.org/10.5194/amt-3-1673-2010, https://www.atmos-meas-tech.net/3/1673/2010/, 2010.

Silver, J. A. and Hovde, D. C.: Near-infrared diode laser airborne hygrometer, Rev. Sci. Instrum., 65, 1691, https://doi.org/10.1063/1.1144861, 1994.

Solomon, S., Rosenlof, K. H., Portmann, R. W., Daniel, J. S., Davis, S. M., Sanford, T. J., and Plattner, G.-K.: Contributions of stratospheric 495   water vapor to decadal changes in the rate of global warming, Science, 327, 1219–1223, https://doi.org/10.1126/science.1182488, 2010.

Sonnenfroh, D. M., Kessler, W. J., Magill, J. C., Upschulte, B. L., Allen, M. G., and Barrick, J. D. W.: In-situ sensing of tropospheric water vapor using an airborne near-IR diode laser hygrometer, Appl. Phys. B Lasers Opt., 67, 275–282, 1998.

Sugidachi, T.: New Peltier-based chilled-mirror hygrometer "SKYDEW", GRUAN ICM-10, 2018.

Thornberry, T. D., Rollins, A. W., Gao, R. S., Watts, L. A., Ciciora, S. J., McLaughlin, R. J., and Fahey, D. W.: A two-channel, tunable diode 500   laser-based hygrometer for measurement of water vapor and cirrus cloud ice water content in the upper troposphere and lower stratosphere, Atmos. Meas. Tech. Discuss., 7, 8271–8309, https://doi.org/10.5194/amtd-7-8271-2014, 2014.

Toth, R.: Linelist of water vapor parameters from 500 to 8000 cm^{-1}, http://mark4sun.jpl.nasa.gov/h2o.html.

Tran, H., Ngo, N. H., and Hartmann, J. M.: Efficient computation of some speed-dependent isolated line profiles, J. Quant. Spectrosc. Radiat. Transf., 129, 199–203, https://doi.org/10.1016/j.jqsrt.2013.06.015, 2013.

505 Tuzson, B., Graf, M., Ravelid, J., Scheidegger, P., Kupferschmid, A., Looser, H., Morales, R. P., and Emmenegger, L.: A compact QCL spectrometer for mobile, high-precision methane sensing aboard drones, Atmospheric Measurement Techniques Discussions, 2020, 1–16, https://doi.org/10.5194/amt-2020-102, https://www.atmos-meas-tech-discuss.net/amt-2020-102/, 2020.

UNEP: Montreal Protocol – Kigali Amendment, 2016.

Vaisala: RS41 Specifications, https://www.vaisala.com/sites/default/files/documents/RS41-SG-Datasheet-B211321EN.pdf, accessed Feb.
510 2020, 2020.

Vömel, H., Naebert, T., Dirksen, R. J., and Sommer, M.: An update on the uncertainties of water vapor measurements using cryogenic frost point hygrometers, Atmos. Meas. Tech., 9, https://doi.org/10.5194/amt-9-3755-2016, 2016.

Weissler, G. and Carlson, R.: Vacuum Physics and Technology, ISSN, Elsevier Science, 1980.

Werle, P., Mücke, R., and Slemr, F.: The limits of signal averaging in atmospheric trace-gas monitoring by tunable diode-laser absorption
515 spectroscopy (TDLAS), Applied Physics B, 57, 131–139, 1993.

Zondlo, M. A., Paige, M. E., Massick, S. M., and Silver, J. A.: Vertical cavity laser hygrometer for the National Science Foundation Gulfstream-V aircraft, J. Geophys. Res. Atmos., 115, 1–14, https://doi.org/10.1029/2010JD014445, 2010.